2024 International Conference on Advanced Robotics and Mechatronics (ICARM) | 979-8-3503-8572-4/24/$31.00 ©2024 IEEE | DOI: 10.1109/ICARM62033.2024.10715830

Automated Electromagnetic Manipulation of Micron-Scale Rotors on Unstructured Surfaces in Low Reynolds Numbers

Shihao Zhong, Kailun Bai, Yaozhen Hou, Hen-Wei Huang, Qing Shi, *Senior Member*, *IEEE*, Qiang Huang, *Fellow*, *IEEE*, and Huaping Wang*, *Member*, *IEEE*

***Abstract*— The utilization of magnetic microrotors in low Reynolds number liquid environments holds great promise for a wide range of biomedical applications, owing to their ability to maneuver with flexibility. However, during the movement of the microrotors on solid unstructured surfaces, the interaction with neighboring walls has the potential to generate unpredictable disruptions in its motion. This study proposes an automated electromagnetic manipulation method for guiding micron-scale surface rotors along planar paths at low Reynolds numbers. To this end, we designed a magnetic field drive system using multistage electromagnets, and a double-helix rotor with micrometer-scale dimensions. Additionally, we developed a kinematic model for the microrotor that closely resembles that of wheeled mobile robots and employed a sliding mode motion controller to ensure high-precision path following. Results obtained from simulation and experimentation confirm the efficacy of our proposed method, demonstrating precise following of planar paths.**

I. Introduction

Mobile microrotors, drawing inspiration from microbial structures, possess the capability to disrupt spatiotemporal symmetry within microscale liquid environments characterized by low Reynolds numbers [1], [2]. This disruption enables them to achieve net displacement, rendering them suitable for a diverse range of biomedical applications [3], [4], such as targeting cargo (e.g., drugs, cells) transport, micromanipulation (lab on a chip), and micro/non-invasive surgery (thrombus removal, tumor treatment). Nevertheless, a crucial technical hurdle in actualizing these potential applications lies in the precise manipulation of these microrotors, ensuring their successful navigation through intricate environments while circumventing obstacles and reaching designated target locations [5], [6].

Due to the constraints imposed by its small feature size, the integration of a battery, drive system, sensors, and other essential components into a microrotor presents significant challenges. Consequently, researchers have pioneered various physical field wireless driving techniques [7], [8], including ultrasonic drive, light field/photoelectric field drive, magnetic field drive, and others. Given their capacity to penetrate deep tissues, compatibility with living organisms, and ease of operation, electromagnetic fields have emerged as a widely employed method for manipulating microrotors [3], [9]. The helical robot demonstrates the capability to maneuver within Newtonian and viscoelastic media through the utilization of a rotating magnetic field generated by a permanent magnet [10]. The soft spiral microrobot is driven by a rotating electromagnetic field to achieve targeted cell transport [11]. The utilization of electromagnetic fields to propel helical magnetic devices swimming at a non-zero angle of attack can effectively counteract gravity and achieve flotation [12]. However, all the aforementioned operational tasks rely on an open-loop control strategy that is inadequate in managing perturbations like thermal noise, boundary effects, and fluid drag.

In contrast, closed-loop control strategy is capable of effectively mitigating motion deviations caused by various disturbances, and relevant research has been reported in this regard. Xu et al. developed a motion mode with a fixed tilt angle to counteract the effect of gravity and achieve levitation of the robot and they also employed a chain controller to ensure that the helical robot maintains a straight path [13]. Wu et al. employed an off-line RBF neural network method to adaptively compensate for the effect of gravity and accomplish path following [14]. Liu et al. proposed an online estimation model to compensate for the influence of gravity and achieve motion control of the helical robot [15]. Xu et al. adopted off-line modeling of an ultra-learning machine to realize adaptive angle compensation, achieving more stable suspension and higher precision following control [16]. Nevertheless, when the microrotors is in close proximity to a wall, it can interact with the solid surface and induce random effects on its motion. Therefore, it is crucial to consider motion control at the surface of the microrotors. Barbot et al. employed two proportional-integral-differential controllers to achieve motion control of a helical microrobot on a surface [17]. Hou et al. developed a fuzzy PID controller to enable helical microdrills to follow a specific path on a plane [18].

*Resrach supported in part by the National Key Research and Development Program of China under Grant 2023YFB4705400; in part by the National Natural Science Foundation of China under Grant 62073042, Grant 62222305, and Grant U22A2064; in part by the Beijing Natural Science Foundation under Grant 4232055; in part by the Science and Technology Innovation Program of Beijing Institute of Technology under Grant 2022CX01019; and in part by the Postdoctoral Fellowship Program of CPSF under Grant BX20230459 (Corresponding author: Huaping Wang).

Shihao Zhong and Yaozhen Hou are with the Intelligent Robotics Institute, School of Mechatronical Engineering, Beijing Institute of Technology, Beijing 100081, China (e-mail: 3120235409@bit.edu.cn, 7520230117@bit.edu.cn).

Kailun Bai is with Science and Technology on Space Physics Laboratory, Beijing 100076, China (e-mail: kelenbai@163.com).

Qing Shi, Qiang Huang, and Toshio Fukuda are with the Beijing Advanced Innovation Center for Intelligent Robots and Systems, Beijing Institute of Technology, Beijing 100081, China (e-mail: shiqing@bit.edu.cn; qhuang@bit.edu.cn; tofukuda@nifty.com).

Hen-Wei Huang is with the Laboratory for Translational Engineering, Harvard Medical School, Cambridge, MA 02139, USA (e-mail: hhuang27@bwh.harvard.edu).

*Huaping Wang is with the Key Laboratory of Biomimetic Robots and Systems, Beijing Institute of Technology, Ministry of Education, Beijing 100081, China (phone: +86-10-68917765; e-mail: wanghuaping@bit.edu.cn).

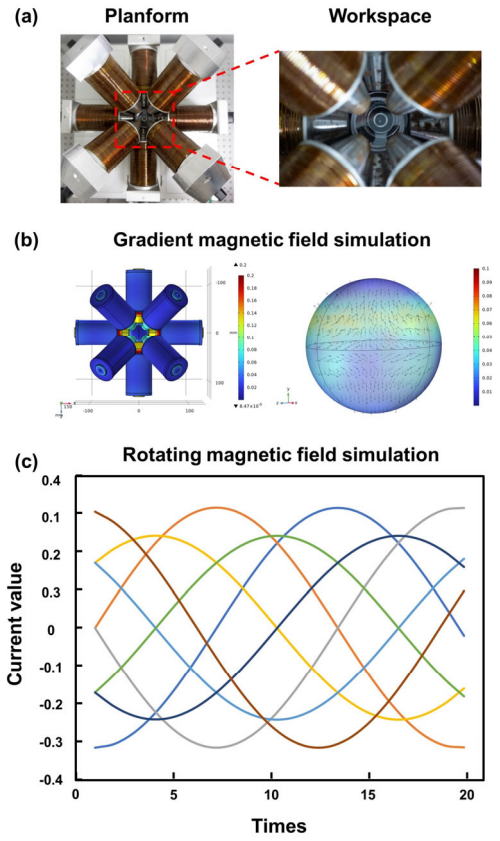

Fig. 1. (a) Top view of the eight-stage electromagnet system and the enlarged view of the workspace. (b) Simulation diagram of gradient magnetic field. (c) Diagram of current variation when a rotating magnetic field is generated. The eight color lines correspond to the current values of the eight electromagnets. The time here represents the sampling sequence.

Zhong et al. combined geometry and model-free control methods to enable the helical microrobot to track any desired plane path [6], [19]. Nevertheless, the aforementioned studies designed a specific spintop motion mode for the microrotor, which ensures that it only has point contact with the solid surface. This reduces the lateral drift caused by friction resistance and wall effect at the micro-scale. However, this approach leads to a reduction in motion speed. Therefore, the motion control of microrotor on solid surfaces is still open to study.

In this study, an automated electromagnetic manipulation method for surface micron-scale rotors to follow planner paths in low Reynolds numbers is proposed. We designed a magnetic field drive system with multistage electromagnets and a double-helix rotor with the micrometer scale will be employed. A kinematic model is developed for the microrotor, which closely resembles the motion model of a wheeled mobile robot. The motion of the microrotor is steered by a sliding mode controller, which enables the system to achieve high path-following precision. The efficacy of our proposed methodology is validated through simulation and experimental outcomes, which demonstrate the capacity to precisely follow planar paths.

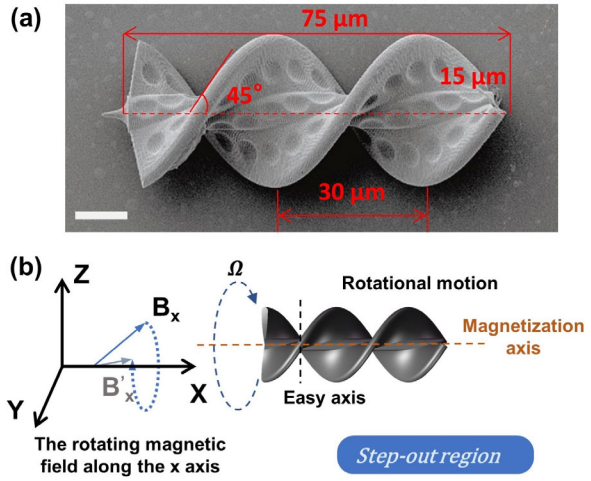

Fig. 2. (a) A physical SEM image of the microrotor. The scar bar is 10 microns. (b) Schematic diagram of microrotor driven by rotating magnetic field.

The structure of this paper is organized as follows. Section II introduces the electromagnet drive system and the kinematics model of the microrotor. Section III analyzes the path following task and designs the controller. The simulation and experimental results are presented in section IV. Section V concludes this article.

II. Models of the System

A. Model of the Eight-Stage Electromagnet System

Fig. 1(a) illustrates an eight-stage electromagnet system that was constructed in-house. The system comprises four horizontal orthogonal coils and four inclined coils, each equipped with a specialized iron core to amplify both the magnetic field strength and gradient. The microcontroller generates a control signal that is transmitted through the driver and applied to the electromagnet at each stage, allowing for programmable magnetic fields generation. The observation device, comprising an optical microscope and a CCD camera, is positioned directly below the geometric center of the class eight-stage electromagnet system. The magnetic fields maintain a fixed strength and frequency, while the camera has a frame rate of 30 frames per second (fps) [6], [18].

The eight-stage electromagnet system can produce magnetic force F_m and magnetic torque T_m to act on magnetic targets in the workspace. The calculation formula is as follows [13], [16]:

$$F_m = (m \bullet \nabla) B \tag{1}$$

$$T_m = m \times B \tag{2}$$

where the magnetic moment of the magnetic object is denoted by m, B represents the magnetic flux density of the magnetic fields, and the gradient operator is represented by ∇.

By adjusting input currents $I_i (i = 1, \ldots, 8)$, the magnetic field can be effectively controlled, allowing for a comprehensive understanding of the relationship between the

current and the magnetic field within the working space, under the assumption of uniform magnetic field distribution. The calculation formula is as follows:

$$B = \left[B_x, B_y, B_z\right]^T = B_0 R\left[I_1, \ldots, I_8\right]^T \tag{3}$$

where B_0 represents the magnetic induction intensity of each coil at the center point of the unit input current, while R is the direction matrix of the multipole coil.

The current value required to generate the desired magnetic field can be solved by the pseudo-inverse operation of the matrix:

$$\left[I_1, \ldots, I_n\right]^T = B_0^{-1} R^{\dagger}\left[B_x, B_y, B_z\right]^T \tag{4}$$

The simulation results of the gradient magnetic field generated by the electromagnetic system are depicted in Figure 1(b). In the experiment, a current of -1A was applied to the four inclined electromagnets, while a current of 0.5A was applied to the four horizontal electromagnets. It is evident from the figure that the magnetic field within the spherical workspace exhibits a near-uniform distribution. In the case of a rotating magnetic field, with a set rotation frequency of 1Hz, Fig. 1(c) displays the variation in the eight-level current.

B. Motion Model of a Microrotor

A double-helix drill-like rotor with the micrometer scale is employed. Hydrogel is utilized as the primary material for preparation, and high-precision optical printing equipment is employed to fabricate the microrotor structure. Magnetic nanoparticles are attached to the surface of microrotor structure. microrotor has a long axis of about 75 microns, a short axis of about 30 microns, a pitch of about 30 microns, and a spiral Angle of about 45 degrees, as shown in Fig. 2(a).

The microrotor can be driven by a rotating magnetic field to produce a net displacement along the long axis with spin motion, as shown in Fig. 2(b). As the magnetic field rotation frequency increases, both the spin speed and forward speed of the microrotor increase correspondingly. However, when the magnetic field rotation frequency surpasses a certain threshold (the out-of-step frequency) the microrotor will no longer be able to rotate synchronously with the magnetic field, ultimately leading to a gradual decrease in forward speed. When the magnetic rotation frequency is lower than the out-of-step frequency, there exists an approximately linear positive correlation between the velocity of the microrotor v and the magnetic field rotation frequency f.

Therefore, the velocity estimation model is:

$$v = k_v f \tag{5}$$

where k_v is the velocity estimation positive gain. The coefficient can be obtained by fitting the experimental data.

In the absence of any perturbations and under ideal conditions, the microrotor exhibits non-holonomic motion because the applied rotating magnetic field does not induce lateral movement [16]. Hence, we consider the kinematics of the microrotor to be similar to that of a unicycle (as shown in Fig. 3). The simplified nonholonomic system we consider describes the motion of a microrotor as follows:

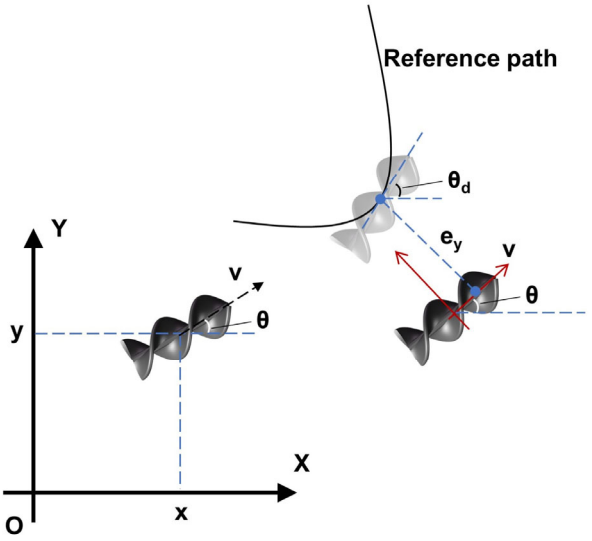

Fig. 3. Lateral and direction errors for path-following task of the microrotor.

$$\begin{cases} \dot{x}(t) = v(t)\cos\theta(t) \\ \dot{y}(t) = v(t)\sin\theta(t) \\ \dot{\theta}(\tau) = w(t) \end{cases} \tag{6}$$

where (x, y) is the global position of the microrotor, θ is the heading angle of the microrotor, and v and w are the forward velocity and angular velocity, respectively.

III. Controller Design

The microrotor may experience lateral drift due to frictional resistance, wall effects, and other micro-scale disturbances resulting from interactions with the wall. To mitigate this issue, it is necessary to design and implement a closed-loop controller capable of restraining or even eliminating the motion deviation caused by these disturbances. The control goal is to make the microrotor reach the target path stably and move along the path, that is to say, the lateral error and direction error need to be eliminated. The error vector in the global frame is defined as:

$$\begin{bmatrix} x_e \\ y_e \\ \theta_e \end{bmatrix} = \begin{bmatrix} x_d - x \\ y_d - y \\ \theta_d - \theta \end{bmatrix} \tag{7}$$

where x_e, y_e, θ_e denote the error of x-axis, y-axis, and an angle, respectively. $\left[x_d, y_d, \theta_d\right]^T$ denotes the desired state vector of the reference path.

The lateral error e_y is quantified as the displacement between the center of gravity of the microrotor and the closest point on the desired path. The directional error e_θ is defined as the angular difference between the direction of motion of the microrotor and the direction of the tangent line of the

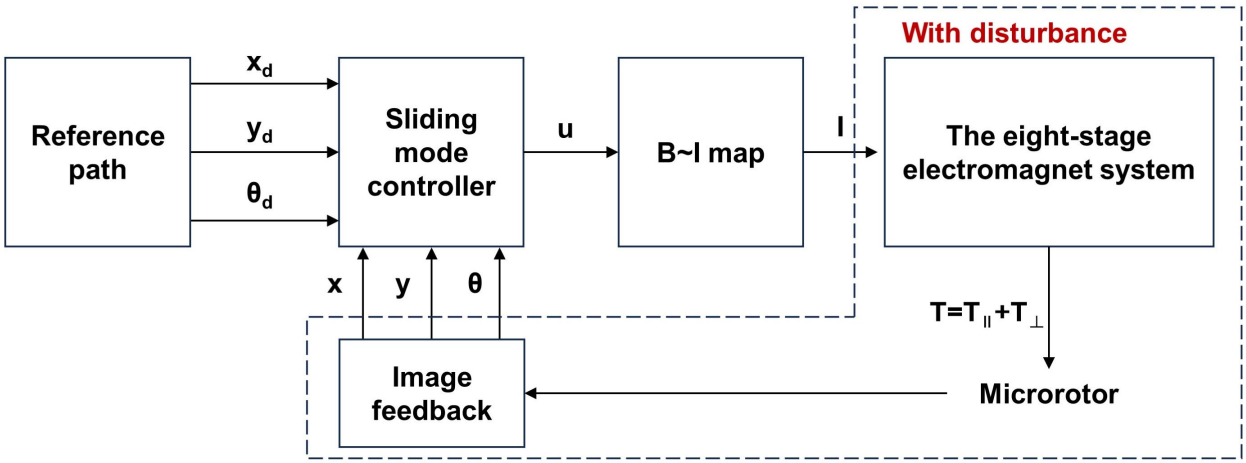

Fig. 4. Control block diagram of microrotor motion in plane.

nearest path point. The error diagram is shown in Fig. 3. In the microrotor coordinate system, the error vector is:

$$\begin{bmatrix} e_x \\ e_y \\ e_\theta \end{bmatrix} = \begin{pmatrix} \cos\theta & \sin\theta & 0 \\ -\sin\theta & \cos\theta & 0 \\ 0 & 0 & 1 \end{pmatrix} \begin{bmatrix} x_d - x \\ y_d - y \\ \theta_d - \theta \end{bmatrix} \tag{8}$$

The corresponding error derivatives are:

$$\begin{cases} \dot{e}_y = v \sin\theta_e \\ \dot{\theta}_e = \dot{\theta}_d - \dot{\theta} = u \end{cases} \tag{9}$$

In order to eliminate the above deviations, a sliding mode controller is designed. In this study, we propose a design for a sliding mode surface that effectively couples the lateral error and directional error, enabling simultaneous convergence of these two error variables. The sliding surface is designed as:

$$s = \dot{e}_y + k_1 e_y + k_2 \operatorname{sgn}(e_y) e_\theta \tag{10}$$

$$\dot{s} = \ddot{e}_y + k_1 \dot{e}_y + k_2 \operatorname{sgn}(e_y) \dot{e}_\theta \tag{11}$$

where k_1 and k_2 are both positive parameters.

In order to guarantee the monotonous convergence of the system states towards the sliding surface within a finite number of steps, we propose a practical and general form of the reaching law, as follows:

$$\dot{s} = -qs - p \operatorname{sgn}(s) \tag{12}$$

where q and p are both positive parameters.

Therefore, the steering control law is:

$$u = \frac{-qs - p \operatorname{sgn}(s) - \ddot{e}_y - k_1 \dot{e}_y}{k_2 \operatorname{sgn}(e_y)} \tag{13}$$

A Lyapunov function may be defined to facilitate the stability analysis of the system:

$$V = \frac{1}{2} s^T s \tag{14}$$

Therefore, its time derivative is:

$$\begin{aligned} \dot{V} &= s\dot{s} \\ &= s\left(\ddot{e}_y + k_1 \dot{e}_y + k_2 \operatorname{sgn}(e_y)\dot{e}_\theta\right) \\ &= s\left(-qs - p \operatorname{sgn}(s)\right) \\ &= -qs^2 - p\frac{s^2}{|s|} \end{aligned} \tag{15}$$

When appropriate non-negative q and p are chosen, $\dot{V}$ can be negative semi-definite.

IV. Simulation and Experiment

To ascertain the efficacy of the proposed control method, we conducted both simulations and experiments. The microrotor is located on the bottom of a petri dish filled with deionized water. The bottom of the dish is an unstructured plane for the microrotor. Video images are processed using the standard OpenCV library.

A. Simulations

The performance of the proposed control method is initially validated through numerical simulations. Specifically, in this simulation, we examine the ability of the control mechanism to guide the microrotor along a linear path, defined as:

$$\begin{cases} x \in [0,5]\ mm \\ y = 1\ mm \\ \theta = 0\ \text{rad} \end{cases} \tag{16}$$

As depicted in Fig. 5, with the guidance of the controller, the resultant motion trajectory effectively converges to the desired path. The black dotted line represents the reference path, and the red dotted line represents the actual motion trajectory. Consequently, the discrepancy in distance errors and direction errors gradually diminish until it ultimately reaches near zero.

Another numerical simulation experiment further verifies the effectiveness of the proposed algorithm. We set the expected path to be a circular path.

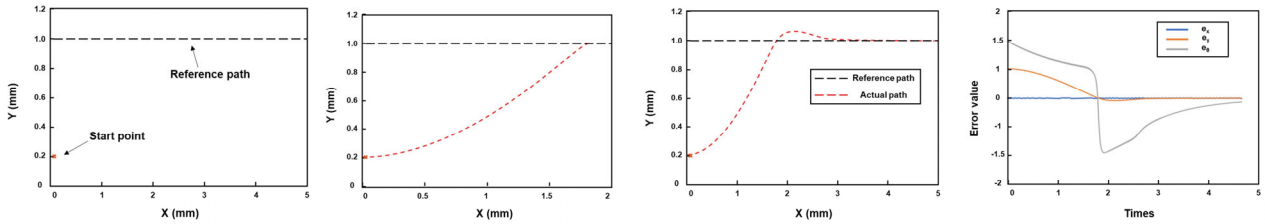

Fig. 5. Simulation process and related errors (distance and direction errors) of the microrotor following the straight path. The black dashed line is the expected path, and the red dashed line is the actual motion path.

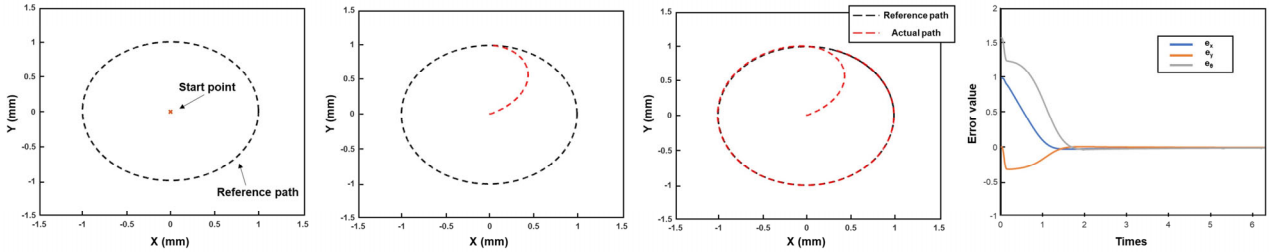

Fig. 6. Simulation process and related errors (distance and direction errors) of the microrotor following the circular path. The black dashed line is the expected path, and the red dashed line is the actual motion path.

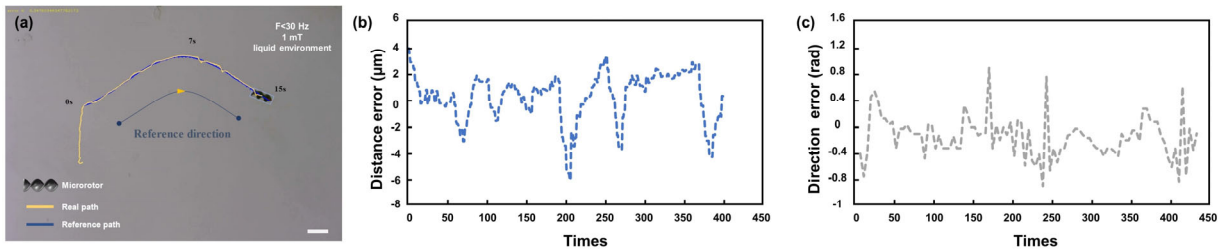

Fig. 7. Microrotor follows a curved path. (a) Schematic diagram of following experimental results. The scar bar is 75 microns. (b) The related distance errors. (c) The related direction errors.

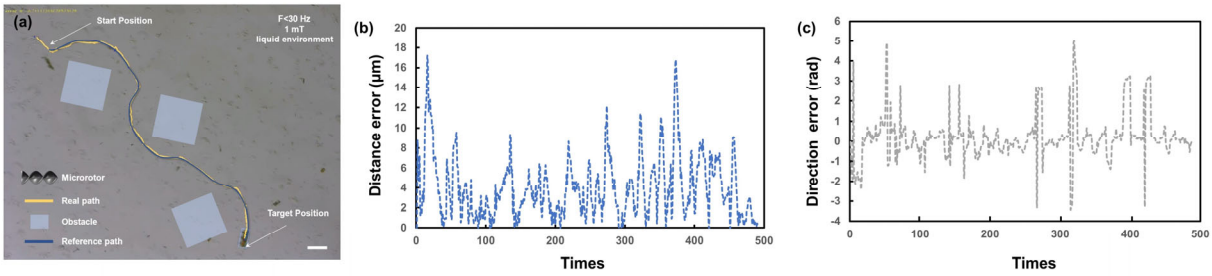

Fig. 8. Path-following experiment with three obstacles in the workspace. (a) Schematic diagram of following experimental results. The scar bar is 75 microns. (b) The related distance errors. (c) The related direction errors.

$$\begin{cases} x = \sin(\theta)\ mm \\ y = \cos(\theta)\ mm \\ \theta \in [0, 2\pi]\ \text{rad} \end{cases} \tag{17}$$

Based on Fig. 6, the black dotted line represents the reference path, and the red dotted line represents the actual motion trajectory. It is evident that both the distance error and the direction error rapidly approach zero. This indicates that the system or algorithm under consideration is effective in minimizing errors related to distance and direction.

B. Experiments

Based on the electromagnet system proposed in section II, we design two path following experiments to further prove the effectiveness of the proposed control method.

Initially, we guide the microrotor along a continuous curved path depicted in Fig. 7(a). The planned path is shown

by dark blue lines, and the actual movement trajectory of the microrotor is illustrated by yellow line. In the experiment, we only controlled the direction of the rotating magnetic field, without changing the magnetic field rotation frequency, and the magnetic field size was 1mT. The subsequent analysis demonstrates the temporal evolution of the microrotor motion state. It is evident from Fig. 7 (b) and (c) that during the ensuing task, both the distance error and direction error gradually converge to nearly zero.

In the second experiment, we established three obstacles within the working space and devise collision-free paths. The primary objective of this experiment entailed ensuring precise adherence of the microrotor to the designated path while successfully circumventing the obstacles. The obstacles are depicted as light blue squares, the planned path is shown by dark blue lines, and the actual movement trajectory of the microrotor is illustrated by yellow lines, as presented in Fig.8 (a). In the experiment, we only controlled the direction of the rotating magnetic field, without changing the magnetic field rotation frequency, and the magnetic field size was 1mT. The experimental results, as showcased in Fig. 8 (b) and (c), present the data pertaining to both distance error and direction error, which gradually converge to nearly zero.

Based on the findings from the conducted experiments, it can be observed that the error consistently approaches zero; however, it is accompanied by noticeable fluctuations. The fluctuation in error can be attributed to two primary factors. Firstly, it arises due to the inherent micro-rotor movement, which exhibits unstable tremors, consequently leading to instability in the micro-rotor's posture. Consequently, this rapid change in visual positioning necessitates frequent adjustments to the magnetic field by the controller, resulting in jitter in control. Secondly, the non-uniform nature of the liquid within the micro-scale environment introduces the possibility of minute impurities mixing with the micro-rotor, thereby causing deviations in the identification of the center of gravity point.

V. Conclusion

In this study, we design a path following control method for a microrotor on a solid surface. In order to drive the micro-rotor, we designed a set of multistage electromagnet combination magnetic field generation system. Based on the motion of the unicycle, the path following kinematics model of the microrotor is established. In order to achieve high precision following task, we designed a sliding mode controller to eliminate motion deviation. Simulation and experiment verify the effectiveness of the proposed method. However, it is worth noting that the error of visual recognition brings instability to the control. Our future work will address this issue.

References

[1] S. Jeon, et al., "Magnetically actuated microrobots as a platform for stem cell transplantation," *Sci. Robot.*, vol. 4, no. eaav4317, 2019.

[2] H. Wang et al., "Data-Driven Parallel Adaptive Control for Magnetic Helical Microrobots with Derivative Structure in Uncertain Environments," *IEEE Trans. Syst. Man Cybern.: Syst.*, early access, doi: 10.1109/TSMC.2024.3374071.

[3] J. Li et al., "Micro/nanorobots for biomedicine: Delivery, surgery, sensing, and detoxification," *Sci. Robot.*, vol. 2, no. eaam6431, 2017.

[4] Y. Dong, L. Wang, V. Iacovacci, X. Wang, L. Zhang, and B. J. Nelson, "Magnetic helical micro-/nanomachines: Recent progress and perspective," *Matter*, vol. 5, no. 1, pp. 77–109, Jan. 2022.

[5] J. J. Abbott, E. Diller, and A. J. Petruska, "Magnetic methods in robotics," *Annu. Rev. Control Rob. Auton. Syst.*, vol. 3, pp. 57-90, 2020.

[6] S. Zhong et al., "Spatial Constraint-Based Navigation and Emergency Replanning Adaptive Control for Magnetic Helical Microrobots in Dynamic Environments," *IEEE Trans. Autom. Sci. Eng.*, early access, doi: 10.1109/TASE.2023.3339637.

[7] B. Ahmad, M. Gauthier, G. J. Laurent and A. Bolopion, "Mobile Microrobots for In Vitro Biomedical Applications: A Survey," *IEEE Trans. Rob.*, vol. 38, no. 1, pp. 646-663, Feb. 2022.

[8] Q. Wang and L. Zhang, "External power-driven microrobotic swarm: from fundamental understanding to imaging-guided delivery," ACS Nano, vol. 15, no. 1, pp. 149-174, 2021.

[9] S. Zhong et al., "Double-Modal Locomotion of a Hydrogel Ultra-Soft Magnetic Miniature Robot with Switchable Forms," *Cyborg Bionic Syst.*, vol. 5, no. 0077, 2024.

[10] D. Mahdy et al., "Experimental characterization of helical propulsion in Newtonian and viscoelastic mediums," *2017 IEEE International Conference on Manipulation, Manufacturing and Measurement on the Nanoscale (3M-NANO)*, Shanghai, China, 2017, pp. 311-314.

[11] E. E. Hunter, E. W. Brink, E. B. Steager and V. Kumar, "Toward Soft Micro Bio Robots for Cellular and Chemical Delivery," *IEEE Rob. Autom. Lett.*, vol. 3, no. 3, pp. 1592-1599, July 2018.

[12] L. -J. W. Ligtenberg et al., "Helical Propulsion in Low-Re Numbers with Near-Zero Angle of Attack," *2023 IEEE/RSJ International Conference on Intelligent Robots and Systems (IROS)*, Detroit, MI, USA, 2023, pp. 2647-2652.

[13] T. Xu, G. Hwang, N. Andreff and S. Régnier, "Planar Path Following of 3-D Steering Scaled-Up Helical Microswimmers," *IEEE Trans. Rob.*, vol. 31, no. 1, pp. 117-127, Feb. 2015.

[14] X. Wu et al., "3-D Path Following of Helical Microswimmers with an Adaptive Orientation Compensation Model," *IEEE Trans. Autom. Sci. Eng.*, vol. 17, no. 2, pp. 823-832, April 2020.

[15] J. Liu et al., "3-D Autonomous Manipulation System of Helical Microswimmers with Online Compensation Update," *IEEE Trans. Autom. Sci. Eng.*, vol. 18, no. 3, pp. 1380-1391, July 2021.

[16] T. Xu, J. Liu, C. Huang, T. Sun and X. Wu, "Discrete-Time Optimal Control of Miniature Helical Swimmers in Horizontal Plane," *IEEE Trans. Autom. Sci. Eng.*, vol. 19, no. 3, pp. 2267-2277, July 2022.

[17] A. Barbot, D. Decanini, and G. Hwang, "Local flow sensing on helical microrobots for semi-automatic motion adaptation," *Int. J. Robot. Res.*, vol. 39, no. 4, pp. 476–489, Mar. 2020.

[18] Y. Hou et al., "Design and control of a surface-dimple-optimized helical microdrill for motions in high-viscosity fluids," *IEEE/ASME Trans. Mechatronics*, vol. 28, no. 1, pp. 429–439, Feb. 2023.

[19] S. Zhong et al., "Path Tracking Control for Helical Microrobots Based on Fusion of Geometric and Model-Free Methods," 2023 IEEE 13th International Conference on CYBER Technology in Automation, Control, and Intelligent Systems (CYBER), Qinhuangdao, China, 2023, pp. 118-123.